

JGR Space Physics



RESEARCH ARTICLE

10.1029/2022JA030294

Key Points:

- Resonance Maps are useful for interpreting resonantly excited Alfvén in complex potential magnetic fields
- Efficient resonant fast-Alfvén wave coupling can occur where the plasma displacement is tangential to the Resonant Zone boundary
- “Toroidal” and “Poloidal” have limited usage in complex magnetic fields. Directions based on the Resonance Map have more utility

Correspondence to:

A. Wright and A. W. Degeling,
anw@st-and.ac.uk;
degeling@sdu.edu.cn

Citation:

Wright, A., Degeling, A. W., & Elsden, T. (2022). Resonance Maps for 3D Alfvén waves in a compressed dipole field. *Journal of Geophysical Research: Space Physics*, 127, e2022JA030294. <https://doi.org/10.1029/2022JA030294>

Received 14 JAN 2022

Accepted 17 MAR 2022

Resonance Maps for 3D Alfvén Waves in a Compressed Dipole Field

Andrew Wright¹ , Alexander W. Degeling² , and Thomas Elsden³ 

¹School of Mathematics and Statistics, University of St Andrews, St Andrews, UK, ²Shandong Provincial Key Laboratory of Optical Astronomy and Solar-Terrestrial Environment, Institute of Space Sciences, Shandong University, Weihai, China,

³School of Mathematics and Statistics, University of Glasgow, Glasgow, UK

Abstract Resonance Maps depict the possible locations and polarizations of resonant Alfvén waves (Field Line Resonances – FLRs) for a given equilibrium and driving frequency. Previously the use of Resonance Maps has been developed for gaining insight into the behavior of Alfvén waves in basic potential magnetic fields that allow the use of an orthogonal field aligned coordinate system. In more general magnetic fields these coordinates do not exist. In this paper we explore the application of Resonance Maps to such equilibria. A number of simulations of resonant Alfvén waves are presented and interpreted using the Maps. We find that Resonance Maps remain useful when some of the constructions used previously are generalised to accommodate the properties of more general magnetic fields. For example, Resonance Maps are able to predict the location and polarisation of Alfvén waves which are driven strongly by fast mode waves using a “tangential alignment condition”. Unusual properties, such as Alfvén waves crossing flux surfaces persist in the more general magnetic fields we consider.

1. Introduction

Almost five decades ago the resonant coupling of fast and Alfvén waves was introduced by Southwood (1974) and Chen and Hasegawa (1974) to explain properties of Ultra-Low Frequency (ULF) pulsations reported by Samson et al. (1971). Initial modeling often adopted simplifications such as a Cartesian geometry and Fourier mode dependences on time and some coordinates to reduce the model to a singular ordinary differential in the radial-like coordinate – a so-called 1D normal mode. Subsequent studies generalised this model to introduce time dependence (Allan et al., 1986; Mann et al., 1995).

Theoretical models were extended to include 2D spatially varying equilibria. Most of these were ‘axisymmetric’ and included analytical normal modes (Thompson & Wright, 1993; Wright & Thompson, 1994) as well as time dependent numerical studies (Lee & Lysak, 1989). There were also 2D non-axisymmetric normal mode studies (Russell & Wright, 2010) as well as time-dependent modeling (Rickard & Wright, 1994; Wright, 1994).

The study of fast and Alfvén wave coupling in 3D is in its infancy, but there is clear evidence that the process continues to operate in both normal mode investigations (Degeling et al., 2010; Kabin et al., 2007; Wright & Elsden, 2016) and time dependent numerical simulations. These simulations use codes specifically designed to study fast and Alfvén wave coupling (Degeling et al., 2018; Elsden & Wright, 2017; Wright & Elsden, 2020) as well codes designed for more general global magnetospheric simulations (Claudepierre et al., 2010; Ellington et al., 2016). Approximate analytical solutions of normal modes have also been derived by Mager and Klimushkin (2021).

In an effort to interpret the results of 3D resonant fast-Alfvén wave coupling Wright and Elsden (2016) introduced the idea of the Resonance Map to show where resonant coupling is possible, and also where it would be strongest. These studies used a potential magnetic field that permitted the use of a global orthogonal field-aligned coordinate system. Elsden and Wright (2020) showed how the Resonance Maps could also be used to understand properties of high- m Alfvén waves (where m is the azimuthal wave number). Analytical studies of high- m Alfvén waves used similar ideas (termed a ‘transparency region’) to describe their properties (Klimushkin et al., 1995, Figure 2; Leonovich & Mazur, 1993, Figure 2).

The use and effectiveness of Resonance Maps has been established for Alfvén waves in equilibrium fields that admit the use of a global orthogonal field-aligned coordinate system. Realistic modeling of planetary

© 2022. The Authors.

This is an open access article under the terms of the [Creative Commons Attribution License](https://creativecommons.org/licenses/by/4.0/), which permits use, distribution and reproduction in any medium, provided the original work is properly cited.

magnetospheres will require more general magnetic fields, and here we consider one possible potential field – namely, the compressed dipole. Such a field does not possess an orthogonal coordinate system, and requires a formulation involving non-orthogonal coordinates (Degeling et al., 2010; Kabin et al., 2007). The aim of this paper is to see if Resonance Maps can be used for such equilibria, and identify how their properties need to be reformulated for a more general magnetic field.

The paper is structured as follows: Section 2 show an example from an equilibrium that permits the use of orthogonal field-aligned coordinates and summaries the established use of Resonance Maps; Section 3 presents results from an equilibrium using a compressed dipole (modeled using non-orthogonal coordinates) and explores the properties and use of Resonance Maps; Section 4 summarizes the paper.

2. Axisymmetric 3D Dipole

Dungey (1954) and Singer et al. (1981) showed how the standing Alfvén wave equation could be written for two limiting cases of azimuthal wavenumber (m): in an axisymmetric 3D dipole field the low m Alfvén wave has plasma displacement, velocity and magnetic field perturbation in the azimuthal direction and is referred to as the ‘toroidal’ Alfvén wave; for large m these quantities are aligned in the direction perpendicular to the background field direction and the azimuthal direction, and is referred to as the ‘poloidal’ Alfvén wave. The difference in the fundamental frequency of the toroidal and poloidal Alfvén waves is around 30%.

Wright and Elsden (2016) showed how these modes could be generalised further to include Alfvén waves that have an arbitrary polarisation angle (θ) between the toroidal ($\theta = 0$) and poloidal ($\theta = \pi/2$) limits. If we identify a field line by its (x, y) coordinates in the equatorial plane, then the natural Alfvén frequency will depend on x, y and θ , i.e., $\omega_A(x, y, \theta)$. Figure 1a shows how ω_A varies smoothly with θ for a given field line. For an axisymmetric background field the toroidal and poloidal ω_A will be extrema of the $\omega_A(\theta)$ curve. For a 3D dipole the toroidal/poloidal frequencies are the maximum/minimum respectively, and these properties persist even if the density is not axisymmetric. This is a result of the magnetic field having reflectional symmetry in a meridian plane, and we consider the properties of such an equilibrium in the next subsection.

2.1. Low- m Alfvén Waves

Figure 1 shows results from an axisymmetric 3D dipole equilibrium. The non-axisymmetric nature of the results comes from the plasma density variation. The density is chosen to give monotonically decreasing toroidal and poloidal frequencies with increasing L -shell, so is representative of the situation at earth outside the plasmasphere. The density varies periodically with the azimuthal coordinate to highlight the 3D nature of the system. On a given field line (at (x, y) , in the equatorial plane), the Alfvén frequency (ω_A) will depend on the polarisation angle (θ). The variation of $\omega_A(\theta)$ is shown in Figure 1a for the field line at $(x, y) = (8.0, 0)$. Note that the maximum ω_A always has a toroidal polarisation, and the minimum ω_A is always poloidally polarised. The horizontal red line corresponds to the driving frequency used in this subsection ($\omega_d = 0.32$). An Alfvén wave that responds resonantly to such a driver will need to have a specific polarisation ($\theta = \theta_r$, where θ_r is the resonant polarisation angle) such that

$$\omega_A(x, y, \theta_r) = \omega_d, \quad (1)$$

and corresponds to the intersections of the red and black lines in Figure 1a.

The Resonance Map was introduced by Wright and Elsden (2016) to aid with interpreting the Alfvén wave response in simulations: there are field lines where it is possible to find values of θ_r so that Equation 1 is satisfied – these field lines are in the ‘Resonant Zone.’ (The field line used to construct Figure 1a is one such field line.) Conversely there are field lines where $\min(\omega_A) > \omega_d$ or $\max(\omega_A) < \omega_d$ and it is not possible to satisfy Equation 1 – the ‘Non-Resonant Zone.’ The boundaries of the Resonant Zone are where $\min(\omega_A) = \omega_d$ and $\max(\omega_A) = \omega_d$, and for an axisymmetric field this is the same as ω_d matching the poloidal or the toroidal Alfvén frequencies.

The azimuthal variation of the plasma density causes the boundaries of the Resonant Zone to move across L -shells – as shown in red in Figure 1b. Inside this zone are several black paths termed ‘resonant contours’ or ‘resonant paths.’ These have the property that at any (x, y) the tangent to the resonant contour makes an angle θ to the azimuthal direction such that Equation 1 is satisfied. In other words if the Alfvén wave’s plasma displacement is

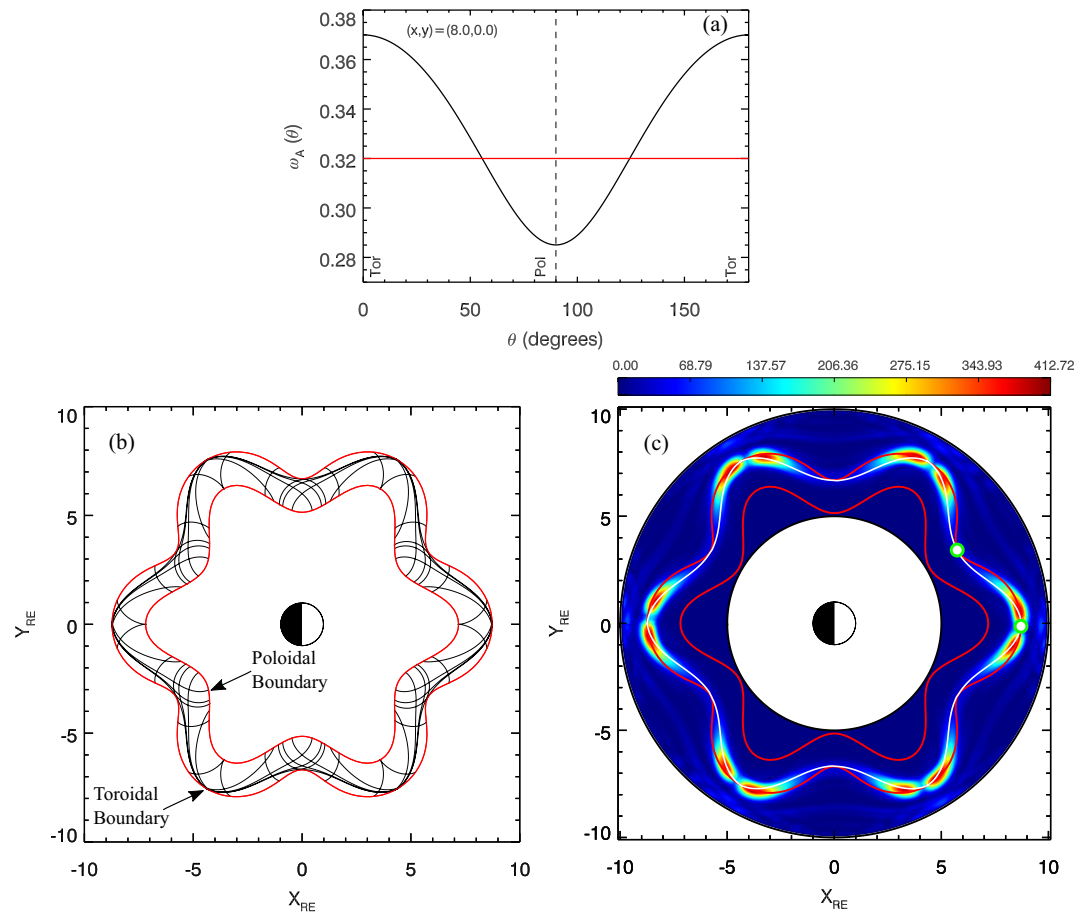


Figure 1. Plots for an axisymmetric 3D dipole with non-axisymmetric density: (a) the variation of ω_A with polarisation angle θ for the field line passing through the equatorial plane at $(8.0, 0)$. The red line indicates the value of the driving frequency ($\omega_d = 0.32$) used in the simulation; (b) the Resonance Map for the system with $\omega_d = 0.32$; (c) magnitude of the field aligned vorticity in the equatorial plane of the corresponding normal mode. The white circles with green edges denote examples of locations where the equilibrium is locally 2D (independent of azimuth).

along the tangents of these lines, then the Alfvén wave will be resonant. Notice how on the outer/toroidal boundary the black lines turn to have an azimuthal orientation as they approach it. In contrast, as these paths approach the inner/poloidal boundary they adopt a radial alignment.

Wright and Elsden (2016) established various criteria for identifying which resonant paths in the Resonance Map would have the largest Alfvén wave response. The criteria relevant to Figure 1 relate to regions where the equilibrium is “locally 2D,” i.e., the derivative of the equilibrium with respect to the azimuthal coordinate is zero. This occurs where the Resonant Zone boundaries have their extrema in radial distance and a couple of instances are denoted by white dots with green edges in Figure 1c. At these locations we expect the normal 2D axisymmetric equilibrium results to apply: the resonant Alfvén waves should have a toroidal polarisation and be excited preferentially at the radial extrema of the toroidal Resonant Zone boundary.

The magnitude of the field-aligned component of vorticity in the equatorial plane for a normal mode with $\omega_d = 0.32$ (shown in Figure 1c) is an indicator of the resonant Alfvén wave, which has a finite width due to the presence of dissipation. (In the equatorial plane the field-aligned vorticity is found from finite differencing the single fluid MHD velocities (v_x and v_y) evaluated in the simulation: $\partial v_y / \partial x - \partial v_x / \partial y$.) The Alfvén wave response will be due to various factors (see Equation 25 of Elsden and Wright (2017)) such as the strength of the fast mode magnetic pressure gradient along the resonant paths, the plasma density and the Alfvén frequency gradient. Evidently these factors favor driving FLRs at the site of the white dot at larger radial distance. To help guide the eye, a single resonant path is plotted on the vorticity panel in Figure 1c in white: it starts at the

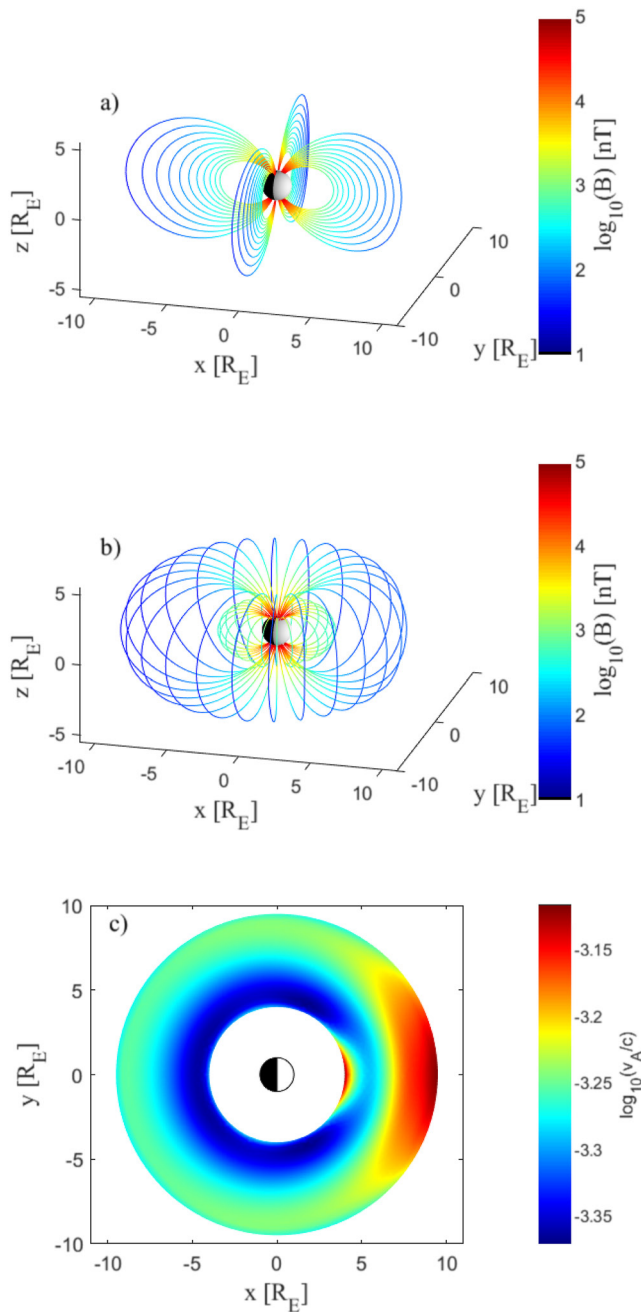


Figure 2. Structure of the compressed dipole equilibrium: (a) and (b) selected field lines; (c) Alfvén speed in the equatorial plane.

we do not attempt to compare directly with observations, but aim to provide a clear understanding of the physics operating. For this reason certain properties are assumed to either simplify the modeling or promote the clearest simulation results. For example, dipole tilt has been omitted and the density is held constant along a field line. However, the Alfvén speed variation shown in Figure 2c provides a realistic variation in Alfvén frequencies with L -shell.

In a compressed dipole field analytical expressions for the various scale factors are not available. To work out the scale factors we (a) choose a polarisation orientation in the equatorial plane and introduce a transverse coordinate (β') along it; (b) take two field lines with a small separation in β' and trace them using a Runge-Kutta scheme;

point on the toroidal boundary with the minimum radial distance, and as it is traced approaches close to the location on the toroidal boundary at maximum radial distance. This situation is similar to a more strongly non-axisymmetric case shown in Figure 10 of Wright and Elsden (2016). The FLRs tend to be trapped between the white line and the outer (toroidal) boundary, and most focused around the outer white dot.

2.2. High- m Alfvén Waves

The construction of a Resonance Map does not make any assumption about whether the Alfvén waves are high or low m . However, the value of m will affect how the Resonance Map is used to interpret Alfvén wave behavior. For low- m the previous subsection and Elsden and Wright (2017) illustrate their usage. For high- m waves in an axisymmetric field the normal mode solution has been considered by (Leonovich & Mazur, 1993) and (Klimushkin et al., 1995) whose analytical treatment showed that the wave would align with the resonant paths we show in the Resonance Map.

In an axisymmetric field the high- m initial value problem was studied by Elsden and Wright (2020). Their results showed that the high- m Alfvén waves would have a poloidal polarisation initially. Subsequently the Alfvén wave would travel along the paths from the poloidal boundary of the Resonant Zone toward the toroidal boundary changing their polarisation continually as they progress. It is surprising that Alfvén waves, noted for their field-aligned propagation of energy and group velocity, are able to behave in a fashion that allows them to cross to neighboring field lines. (See Elsden and Wright (2020) for more discussion of the physics of how this process operates.)

3. Compressed Dipole

In Section 2 the Resonance Map was applied to a 3D Dipole which allows the use of orthogonal field-aligned coordinates. In this section we explore whether Resonance Maps remain valid for more complex magnetic fields for which orthogonal coordinates do not exist. For example, compressed dipole field models provide a useful approximation to the dayside near-Earth magnetosphere that in general do not have an orthogonal field-aligned coordinate system. Alternative (but qualitatively similar) fields have been employed Kabin et al. (2007) and Degeling et al. (2010). We produce a simple compressed dipole field by adding an image dipole at $x = 30 R_E$ that is 9.6463 times stronger than the Earth's to give the subsolar magnetopause at $x = 10 R_E$.

Figure 2 shows the geometry of selected magnetic field lines connected to the earth. Note how the field lines in the noon and midnight meridians are very different: the compression of field lines on the dayside is evident. The Alfvén speed in the equatorial plane is also shown in Figure 2. In this paper

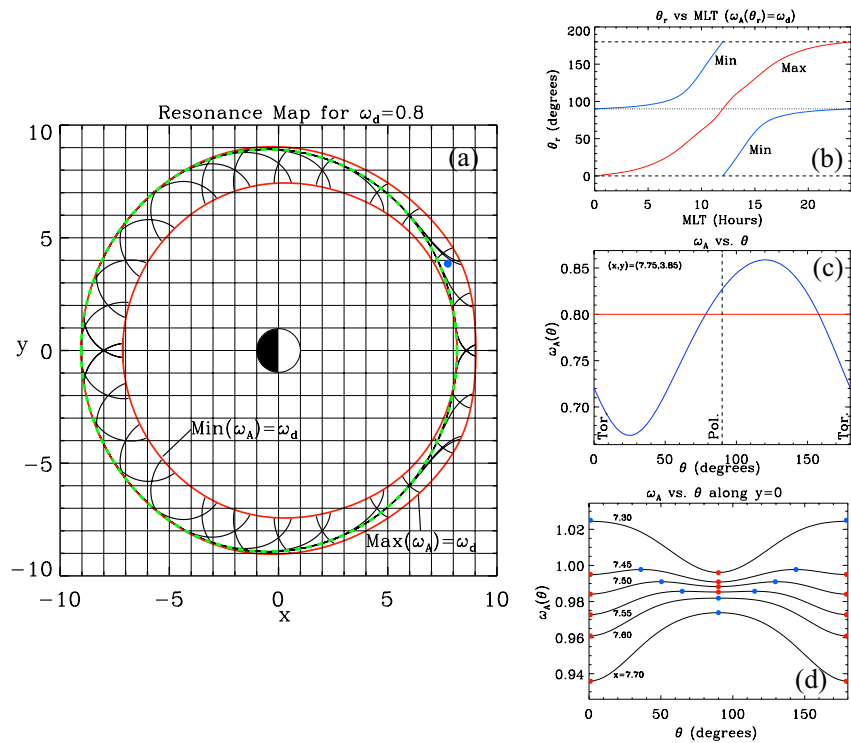


Figure 3. (a) The Resonance Map for the compressed dipole. The red lines indicate the boundaries of the Resonant Zone. The black lines denote resonant paths whose tangents are at the resonant polarisation angle θ_r such that Equation 1 is satisfied. The dashed green line is the favored resonant path for a low- m mode. (b) The variation of θ_r on the boundaries of the Resonant Zone with MLT. The dashed line is the corresponding variation in an axisymmetric dipole (like in Figure 1) for the $\text{Max}(\omega_A) = \omega_d$ boundary and the dotted line for the $\text{Min}(\omega_A) = \omega_d$ boundary. (c) The variation of ω_A with polarisation angle θ for the field line at $(x, y) = (7.75, 3.85)$, indicated by the blue dot in panel (a). The red line indicates the value of ω_d used in the resonance map. (d) The variation of ω_A with θ for several locations on the x axis. The blue dots indicate local maxima and the red dots local minima.

(c) work out the normal separation of the field lines as a function of path length (s) and use this to give the scale factor $h_\beta(s)$; (d) use the solenoidal constraint to work out the effective scale factor $h_a(s)$; Equation 21 of Wright and Elsden (2016)) and solve the corresponding Alfvén wave equation (their Equation 23) for ω_A .

The details of how Step (3) above is achieved are as follows: we have a central field line along which we wish to evaluate the scale factors, and use two additional field lines that are situated symmetrically either side of the central field line. The intersections of the three field lines with the equatorial plane corresponds to three points that are chosen to be colinear and are aligned with the desired polarisation. To calculate the separation of the field lines along the β' direction out of the equatorial plane we choose a point on the central field line and calculate the equation of the plane through this point that is normal to the background field. The points of intersection of the other two field lines with this plane are identified and the distance between them used to determine the separation of the field lines. For this numerical estimate to be reliable the points of intersection of the three field lines with this plane should remain close to colinear, which requires the original separation in the equatorial plane be sufficiently small. To produce the Resonance Maps for the Compressed Dipole field we used an equatorial separation of 2×10^{-4} . To check colinearity was satisfied to a high degree out of the equatorial plane we determined the angle between the two line segments connecting the outlying field lines to the central one. These deviated from linear by typically $\sim 10^{-5}$ of a degree or less, which is more than sufficient for our purposes.

We shall see that the compressed dipole Resonance Map has a number of differences to that from a single dipole, and for this reason have chosen a density variation that gives, at first sight, a rather simple looking Map shown in Figure 3a. In a compressed dipole the boundaries of the Resonant Zone are no longer identified by equating the toroidal and poloidal frequencies with ω_d , rather they are now identified by locating field lines for which $\text{min}(\omega_A) = \omega_d$ and $\text{max}(\omega_A) = \omega_d$. This represents a generalization of the criteria used in axisymmetric fields.

The compressed magnetic field has symmetry across the noon and midnight meridian planes, so at these locations the maximum and minimum $\omega_A(\theta)$ will have either a toroidal or poloidal polarisation and allows us to note some similarities with the axisymmetric dipole. In particular, the Resonance Maps for the 3D dipole (Figure 1b) and the compressed dipole (Figure 3a) are similar at midnight: the resonant paths leave the outer boundary with a toroidal polarisation and approach the inner boundary with a poloidal polarisation.

For the compressed dipole the situation at noon is actually reversed: the resonant paths (black lines) at the outer boundary now have a poloidal alignment and at the inner boundary have a toroidal alignment. A careful examination of the orientation of the resonant paths on the inner boundary show they start at midnight with a poloidal (90°) polarisation, and as we move through dawn to noon the orientation changes smoothly to toroidal ($0/180^\circ$). Figure 3b shows the variation of polarisation angle with magnetic local time (MLT) for both the outer (max ω_A) and inner (min ω_A) boundaries. This behavior is not possible in an axisymmetric field, and the dotted/dashed lines show the corresponding MLT dependence for the inner/outer boundaries for this case.

As we move in MLT for the compressed dipole field the values of the resonant polarisation angles for min and max ω_A change smoothly – as shown in Figure 3b. This is also true as we move from the inner to the outer boundary at fixed MLT. The variation of $\omega_A(\theta)$ is shown in Figure 3c for a point at 14 MLT in the middle of the Resonant Zone (shown by the blue dot in panel (a)). It is evident how the location of the extrema are not confined to toroidal and poloidal polarizations. (The vertical lines at $\theta = 0^\circ, 90^\circ, 180^\circ$ indicate the toroidal and poloidal polarizations where the maximum and minimum frequencies are constrained to occur for an axisymmetric dipole – see Figure 1a.) In Figure 3c the red horizontal line (indicating the value of ω_d) and its intersections with the $\omega_A(\theta)$ curve identify two resonant polarisation angles for this location ($\theta_r = 78.5^\circ$ and 158°).

The ideas developed so far allow us to predict some unusual behavior in the noon meridian. We have established that the symmetry of the field here for both axisymmetric and compressed dipoles means the maximum and minimum $\omega_A(\theta)$ must have a toroidal or poloidal polarisation. For the single axisymmetric dipole the situation is unremarkable: the maximum/minimum ω_A correspond to the toroidal/poloidal polarizations, respectively. Plots of $\omega_A(\theta)$ look like those in Figure 1a for every point along the x axis.

The situation for the compressed dipole at noon is very different to the axisymmetric case (as seen in the results of Kabin et al. (2007)). Figure 3b shows how, for the compressed field lines near the magnetopause, the maximum $\omega_A(\theta)$ has a poloidal polarisation ($\theta_r = 90^\circ$). If we were to move along the x axis toward the earth the effect of the image dipole and compression becomes progressively less, and we revert to the usual axisymmetric result where the maximum $\omega_A(\theta)$ has a toroidal polarisation. This begs the question: if we move along the x axis at noon how can we switch from having the max/min at $\theta = 0^\circ/90^\circ$ to $\theta = 90^\circ/0^\circ$ when the location of the extrema cannot move in θ ?

The answer lies in unusual bifurcatory behavior: we find additional extrema appear to affect the transition, and Figure 3d illustrates this. Panel (d) is a plot of $\omega_A(\theta)$ for several positions along the x axis. (Note that $\theta = 0^\circ$ and 180° is a single solution.) Starting with the upper curve (smallest x) we find a single maximum ($\theta = 0^\circ/180^\circ$, indicated by the red dot) and a single minimum ($\theta = 90^\circ$, indicated by the blue dot), which is similar to the usual axisymmetric dipole. Moving progressively to larger x we work sequentially to lower curves. The next three curves have two maxima and minima, and the final two curves revert to a single maxima and minima – but the locations have interchanged compared to the top curve.

The toroidal and poloidal Alfvén modes of the Hermean Magnetosphere have been reported and modeled by James et al. (2019). The magnetosphere is highly compressed on the dayside by the solar wind, and it is interesting to note that they found the poloidal frequency could exceed the toroidal frequency near noon. This is completely consistent with our results and may be attributed to the effect of compressing dipole field lines: in an uncompressed dipole the separation of field lines in the toroidal and poloidal directions decreases on moving from the equator to the ionosphere in a monotonic fashion, as does the ratio of the poloidal to toroidal separations. It is this ratio that is the key quantity in the Alfvén wave equations (see Equations 2 and 3 of Wright and Elsden (2016)) that makes the poloidal and toroidal modes different. A careful examination of the separation of the outer field lines in the noon meridian in Figure 2a shows the poloidal separation does not decrease monotonically from the equator to the ionosphere, but actually has a maximum midway. This type of distortion will affect the Alfvén frequency and may account for the relative increase of the poloidal frequency. We would also expect behavior like that shown in Figure 3d to occur at Mercury.

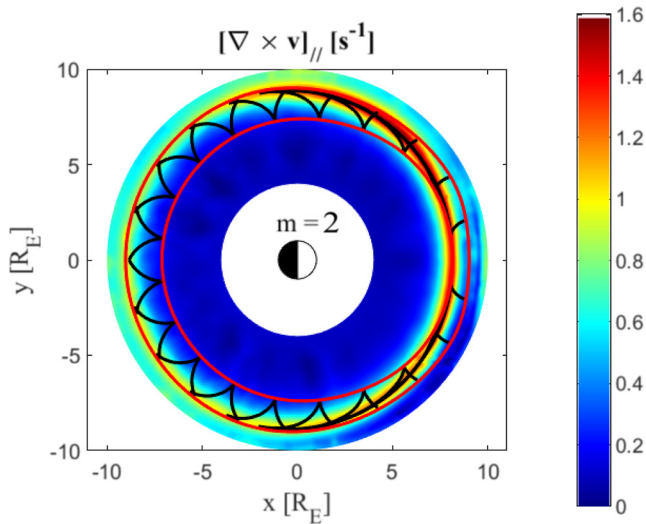


Figure 4. Magnitude of the field aligned vorticity (indicative of Alfvén waves) in the equatorial plane. Red lines indicate the boundary of the Resonant Zone and black lines are resonant paths as presented in Figure 3a.

We now establish whether the Resonance Maps are useful for interpreting simulations of resonant Alfvén waves in a compressed dipole field.

3.1. Low- m Field Line Resonance

Figure 4 shows normal mode results from the code described in Degeling et al. (2018), in which the background magnetic field and plasma density profiles have been adjusted to correspond with those used in the previous section. For the purposes of calculating the normal mode we only consider the domain inside a circle of radius $9.5 R_E$ in the equatorial plane. The field lines threading this circle form the outer surface of our domain. A magnetic pressure perturbation is applied to the surface that is proportional to $\exp i(\omega_d t - m\phi)$, and we take $m = 2$ and $\omega_d = 0.8$ mHz. Further details of the code, governing equations and boundary conditions relevant to this section are given in Appendix A.

The black resonant paths in the Resonance Map in Figure 3a have been replotted as the black lines in Figure 4 which shows the magnitude of the field aligned vorticity. It is evident that the Resonance Map can be used to provide a resonant path that starts at noon on the inner boundary and moves to the outer boundary at midnight and follows the bright red ridge indicative of the resonant Alfvén wave – but why this particular path? We can use the criterion identified by Wright and Elsden (2016): if there are regions where

the field is locally 2D (such as at noon and midnight) we can apply the usual 2D/axisymmetric theory here, and will find the resonant Alfvén wave has a toroidal polarisation. Hence the Alfvén waves should be toroidal on both the inner boundary at noon and the outer boundary at midnight. This particular path (shown as the green dashed line in Figure 3a) is also special in a topological sense – it is a separatrix. Resonant paths that asymptote to the separatrix but lie outside/inside the separatrix all connect to the outer/inner Resonant Zone boundary (Mager & Klimushkin, 2021).

3.2. Low- m Field Line Resonance (No Symmetry)

The previous subsection showed how a 3D equilibrium with points where the medium is “locally 2D” could be used to determine the sites of strong coupling using the criteria familiar from 2D FLR theory: the strongest resonant Alfvén wave will have a toroidal polarisation and be located on the toroidal boundary of the Resonant Zone. It is natural to ask where the strongest resonant coupling occurs in a more general medium where locally 2D regions do not exist, and how the locally 2D criterion generalizes.

We use the same magnetic field as in the previous section and focus on a relatively small section of the equatorial plane centered on $(x, y) = (5, 5)$ where the field is highly distorted and the maximum and minimum values of ω_A have polarizations far from toroidal and poloidal (similar to as shown in Figure 3c). The Alfvén speed is shown in Figure 5a and has been produced by adding a localized density enhancement centered on (5,5) which is, again, held constant along a field line. The simulation is driven in a similar fashion to the previous subsection, except that the driving frequency is now $\omega_d = 0.9$ mHz.

Figure 5b shows the corresponding Resonance Map. Note that for $\omega_d = 0.9$ mHz there is only one Resonant Zone boundary ($\min(\omega_A) = \omega_d$) shown in red, and selected permissible resonant paths are shown in black. The “locally 2D” criterion cannot be applied to this Map. We note that this condition (that the Alfvén wave polarisation be toroidal and occur on the toroidal boundary) actually requires the polarisation to be tangential to the boundary, and suggests the following generalization: the strongest Alfvén wave coupling will occur on the boundaries of the Resonant Zone ($\text{Min/Max}(\omega_A) = \omega_d$) where the Alfvén wave polarisation is such that the plasma displacement is tangential to the boundary. The blue dots in Figure 5b indicate points on the boundary where this criterion is met.

Simulation results are shown in Figure 5c which display the absolute value of parallel vorticity in the equatorial plane on a logarithmic scale. The blue dots in panel (b) clearly identify where the strongest coupling occurs, and lends support to the generalised criterion we propose. Intuitively this condition is conducive to supporting Alfvén

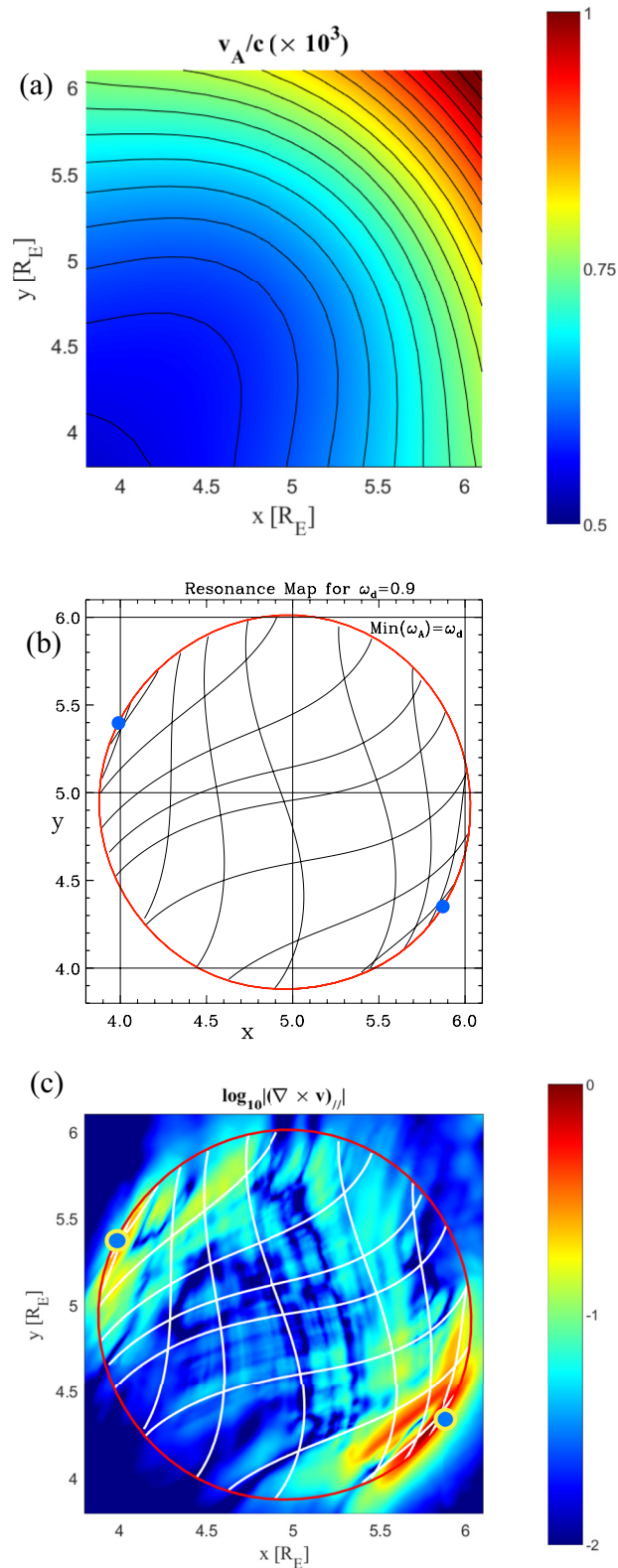


Figure 5. Properties of a low- m FLR where there is no locations which are “locally 2D”: (a) variation of the Alfvén speed in the equatorial plane; (b) the corresponding Resonance Map for $\omega_d = 0.9$ mHz. The blue dots indicate where the “tangential alignment” criterion is satisfied, the black lines are resonant paths (note how the paths begin to become tangential to the boundary as the blue dots are approached); (c) field aligned vorticity in the equatorial plane with resonant paths overlaid (as white lines).

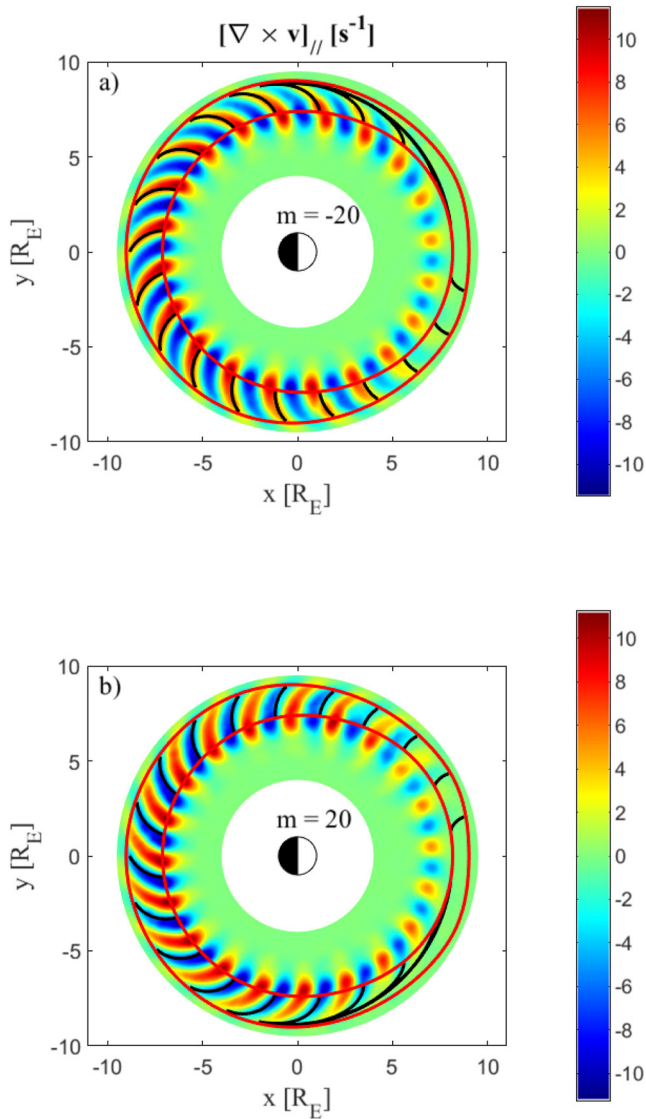


Figure 6. Real part of the equatorial field aligned vorticity when driven with $\omega_d = 0.8$ mHz: (a) has an azimuthal wave number $m = -20$ and (b) uses $m = +20$. In both panels the boundaries of the Resonant Zone are denoted by the red lines, and selected resonant paths by black lines. The equilibrium is the same as that used in subsection 3.1 and Figures 2 and 3.

waves as the plasma displacement is along the boundary and connects to adjacent field lines with a similar polarisation, thus facilitating maintaining $\nabla \cdot \mathbf{b} = \nabla \cdot \mathbf{u} = 0$ for the Alfvén wave field and velocity perturbations.

In contrast, points on the boundary where the resonant polarisation is normal to the boundary will struggle to maintain $\nabla \cdot \mathbf{b} = \nabla \cdot \mathbf{u} = 0$ with a single resonant path: for example, the Alfvén wave magnetic field leads to field lines outside the Resonant Zone where a smaller non-resonant Alfvén wave is expected. Previous results (Figure 7 of Wright & Elsden, 2016) indicate the system maintains the solenoidal constraint by connecting to the other resonant path on the boundary and so continues back inside the Resonant Zone. The smaller amplitude criss-cross features seen in Figure 5c are a product of this behavior.

It should be noted that points where the “tangential alignment condition” is met represent locations that are favorable for the fast mode to drive resonant Alfvén waves. To establish a strong resonant response at the locations also requires the fast mode to have a suitable magnetic pressure gradient with a significant component aligned with the resonant paths (Elsden & Wright, 2017). Moreover in situations where the Resonant Zone encounters simulation boundaries, the conditions imposed there can favor a particular polarisation, and hence select a particular resonant path (Wright & Elsden, 2016).

3.3. High- m Field Line Resonance

Subsection 2.2 described how, in potential magnetic fields that admit the use of orthogonal field aligned coordinates, high- m Alfvén waves can start off with a poloidal polarisation (on the poloidal boundary) and move along resonant paths in the resonant zone and have their polarisation turn toward the toroidal direction. In this subsection we explore whether this type of behavior persists in fields where orthogonal field aligned coordinates do not exist. To this end we use the same equilibrium, and hence Resonance Map, as in Figures 2 and 3.

The normal mode we calculate is different to before in that we take $m = \pm 20$ and we no longer drive the waves through magnetic pressure on the magnetopause. High- m waves are normally thought to be excited through a resonant interaction with drifting ions (Southwood & Kivelson, 1981). As we are using an MHD simulation we mimic the effect of driving by ions by adding a poloidally aligned driving force to the momentum equation. The force is proportional to $\exp(i(\omega_d t - m\phi))$ and localized to the vicinity of the $L = 7$ L -shell. We retain $\omega_d = 0.8$ mHz to allow the use of the Resonance Map in Figure 3a. Figure 6 shows the normal modes corresponding to $m = +20$ and $m = -20$. We have overplotted (black lines) selected resonant paths that the high- m features follow.

Evidently the strongest excitation occurs at midnight. This is most likely because the paths at $L = 7$ at midnight are polarised poloidally so align well with the driving force, which is also situated at $L = 7$. Hence high- m FLRs can be excited very efficiently here. The situation remains similar to this over the nightside (18–6 MLT): Figure 3b shows the polarisation at the inner (minimum ω_A) boundary for these MLTs remains close to 90° (i.e., close to poloidal) and its location remains close to the driving force at $L = 7$, hence there is efficient excitation of poloidal Alfvén waves at the inner boundary over this MLT range.

No Alfvén waves are excited at noon, and we attribute this to the inner boundary having moved slightly away from the driver. The faint traces of vorticity at noon outside of the resonance zone are due to a small non-resonant

response of the field lines at $L = 7$. Moreover, the field lines in the Resonant Zone closest to the driver (those on the inner boundary) have a toroidal polarisation at noon, so will not be excited effectively by a poloidal driving force.

As we move from dawn or dusk toward noon the separation of the inner boundary and the driver location gradually increases, as does the misalignment of the Alfvén wave polarisation on this boundary with the direction of the poloidal driving force (see Figure 3b). For these reasons the amplitude of the resonant Alfvén waves decreases as noon is approached.

Elsden and Wright (2020) showed how the time-dependent initial value problem, if initialized with an azimuthally standing high- m poloidal Alfvén wave, would split subsequently into two Alfvén waves - one following resonant paths that curved to the west, and the other following paths curving to the east. They also showed that if the initial condition had phase motion in the azimuthal direction, then only one set of paths were followed. This is consistent with the modes in Figure 6 following either the set of paths that sweep eastwards or those that sweep westward on leaving the inner boundary.

The normal mode results in Figure 6a have a phase motion in the westward (clockwise) direction, whilst the motion for Figure 6b is eastward (anti-clockwise). Hence we would expect ions to interact most strongly with the mode in Figure 6a as ions also drift westward. Note that the polarisation angle of the FLRs varies with L -shell as will the Alfvén wave's Electric field (which is perpendicular to the black resonant paths in Figure 6) and this will affect how strongly ions can couple to high- m FLRs.

4. Concluding Remarks

We have shown that Resonance Maps can be used for understanding resonantly excited Alfvén waves in complex potential magnetic fields that do not admit the use of an orthogonal field aligned coordinate system. Some generalisations are needed in the construction and application of Resonance Maps compared to simpler magnetic fields where an orthogonal coordinate system does exist.

In axisymmetric magnetic fields the boundaries of the Resonant Zone are where the toroidal and poloidal Alfvén frequencies match the driving frequency. This is not the case in more general magnetic fields. Indeed, toroidal and poloidal directions (which are a property of an artificial coordinate system) have little meaning in a more general magnetic field. Instead, it is more useful to identify the maximum and minimum ω_A on each field line, as these are properties of the equilibrium, rather than being tied to an imposed coordinate system. The boundaries of the Resonant Zone are where the driving frequency matches either the maximum or minimum ω_A . Moreover, the Alfvén wave polarisation on these boundaries will not, in general, be poloidal or toroidal (as is it for an axisymmetric field).

In more general potential fields (e.g., lacking axisymmetry) efficient fast-Alfvén wave resonant coupling occurs at locations on the Resonant Zone boundaries where the resonant polarisation corresponds to the plasma displacement being tangential to the boundary (a “tangential alignment condition”). This criterion is a generalization of the “locally 2D” condition identified for simpler magnetic fields.

For high- m Alfvén waves the polarisation will not necessarily be poloidal on the Resonant Zone boundary. The high- m waves will also drift across L -shells and their polarisation will change as they do so. The efficiency of the interaction between ions and high- m waves depends on the ions and waves being on the same field lines and also having a suitably oriented electric field. Hence it would be worth reexamining existing models of this process to assess the impact of the new properties of waves expected in 3D magnetic fields.

Appendix A

The model for MHD waves in a compressed dipole magnetic field has been described previously in (Degeling et al., 2010, 2018), so only a brief overview is given here. This model uses the covariant formalism (D'haeseleer et al., 1991) to express the MHD wave equations in a general field-aligned coordinate system applicable to background field magnetic field models in which $\mathbf{B} \cdot \nabla \times \mathbf{B} = 0$ (i.e., there is no equilibrium field-aligned current). In this case, a curvilinear coordinate system (α, β, γ) may be constructed in which $\mathbf{B} = B_{0E} \sigma \nabla \gamma = B_{0E} \nabla \alpha \times \nabla \beta$, where B_{0E} is a constant, and spatial variations in $\sigma(\alpha, \beta, \gamma)$ define currents perpendicular to \mathbf{B} (since $\mu_0 \mathbf{J} = B_{0E} \nabla \sigma \times \nabla \gamma$).

For the case of an image dipole vacuum field as described in Section 3, σ is set equal to one and γ is given by the sum of the Earth dipole and displaced image dipole scalar potentials. Note that in this system, $\nabla\gamma$ is orthogonal to both $\nabla\alpha$ and $\nabla\beta$, however $\nabla\alpha$ and $\nabla\beta$ are not necessarily orthogonal to each other. A vector \mathbf{V} may be expressed in terms of its covariant components by $\mathbf{V} = V_\alpha \nabla\alpha + V_\beta \nabla\beta + V_\gamma \nabla\gamma$. The covariant components of the wave electric field \mathbf{E} are then given by solving the following coupled PDE equations:

$$\left(\frac{1}{\sigma} \mathbf{G} \cdot \begin{pmatrix} E_\alpha \\ E_\beta \end{pmatrix} \right)' - \frac{\sqrt{g}}{v_A^2} \mathbf{G} \cdot \begin{pmatrix} \dot{E}_\alpha \\ \dot{E}_\beta \end{pmatrix} - \frac{1}{\sigma} \begin{pmatrix} -\partial/\partial\beta (b_\gamma \sigma) \\ \partial/\partial\alpha (b_\gamma \sigma) \end{pmatrix} = \sqrt{g} \begin{pmatrix} \nabla\alpha \\ \nabla\beta \end{pmatrix} \cdot (\mu_0 \mathbf{J}_{ext}) \quad (\text{A1})$$

where $E_\gamma = 0$ for ideal MHD, dashes and dots represent partial differentiation with respect to γ and t respectively, \mathbf{J}_{ext} is an externally applied current source for driving waves, b_γ is the covariant field-aligned component of the wave magnetic field, $\sqrt{g} = (\nabla\alpha \times \nabla\beta \cdot \nabla\gamma)^{-1}$ and \mathbf{G} is a 2×2 tensor given by:

$$\mathbf{G} = \begin{pmatrix} \nabla\alpha \cdot \nabla\alpha & \nabla\alpha \cdot \nabla\beta \\ \nabla\alpha \cdot \nabla\beta & \nabla\beta \cdot \nabla\beta \end{pmatrix} \quad (\text{A2})$$

The field-aligned component of Faraday's law gives $\dot{b}_\gamma = -\sigma (\partial E_\beta / \partial\alpha - \partial E_\alpha / \partial\beta)$, and provides closure to Equation A1. Normal modes with frequency ω are modeled by assuming the wave parameters and source vary as $\exp(i\omega t)$, such that \ddot{E} terms in Equation A1 are replaced by $-\omega^2 E$. A small imaginary part is added to ω representing ionospheric dissipation of power due to a finite (but assumed large) ionospheric Pedersen conductance.

The resulting spatial PDE equations are solved implicitly by means of operator splitting, with a Galerkin spectral method in the field-aligned direction and a 2D finite element method in the perpendicular directions. For the former, a set of (up to 10) orthogonal Chebyshev-type basis functions with nodes enforced at the ionosphere (satisfying the infinite conductivity boundary condition) and anti-nodes in the equatorial plane are used to represent electric field variations in the field-aligned direction. For the latter, the complex amplitudes weighting these basis functions are solved on an unstructured triangular mesh, defined in the equatorial plane between a specified inner and outer boundary (e.g., between $L = 4$ and $L = 9.5$). The inner and outer boundary conditions in the model are of Dirichlet type, with all amplitude components set to zero at the inner boundary in all cases. At the outer boundary for a low m wave driver (as shown in Figures 4 and 5), a constant amplitude perturbation with phase variation $\exp(-im\phi)$ is given to the lowest order basis functions for the component of \mathbf{J}_{ext} tangential to the outer boundary. This is equivalent to applying a magnetic pressure perturbation on the boundary. In the case of a high m driver located interior to the magnetosphere (as shown in Figure 6, in which the driver is centered at $L = 7$), the outer boundary components are set to zero.

Data Availability Statement

Simulation data can be accessed online at: https://figshare.com/authors/Tom_Elsden/4743264.

Acknowledgments

A. Wright was partially funded by the Science and Technology Facilities Council (STFC) grant (ST/N000609/1). T. Elsdén is funded by a Leverhulme Trust Early Career Fellowship (ECF-2019-155) and the University of Glasgow. A. Degeling is supported by the National Natural Science Foundation of China (41774172), and gratefully appreciates collaborative discussions with R. Rankin and the use of facilities at University of Alberta during this work. The research in this paper was completed as part of the activities of an International Team sponsored by the International Space Science Institute (ISSI, Bern). The authors are grateful to ISSI for supporting this work.

References

- Allan, W., White, S. P., & Poulter, E. M. (1986). Impulse-excited hydromagnetic cavity and field-line resonances in the magnetosphere. *Planetary and Space Science*, 34, 371–385. [https://doi.org/10.1016/0032-0633\(86\)90144-3](https://doi.org/10.1016/0032-0633(86)90144-3)
- Chen, L., & Hasegawa, A. (1974). A theory of long-period magnetic pulsations: 1. Steady state excitation of field line resonance. *Journal of Geophysical Research*, 79, 1024–1032. <https://doi.org/10.1029/JA079i007p01024>
- Claudepierre, S. G., Hudson, M. K., Lotko, W., Lyon, J. G., & Denton, R. E. (2010). Solar wind driving of magnetospheric ULF waves: Field line resonances driven by dynamic pressure fluctuations. *Journal of Geophysical Research*, 115, A11202. <https://doi.org/10.1029/2010JA015399>
- Degeling, A. W., Rae, I. J., Watt, C. E. J., Shi, Q. Q., Rankin, R., & Zong, Q.-G. (2018). Control of ULF Wave Accessibility to the Inner Magnetosphere by the Convection of Plasma Density. *Journal of Geophysical Research: Space Physics*, 123, 1086–1099. <https://doi.org/10.1002/2017JA024874>
- Degeling, A. W., Rankin, R., Kabin, K., Rae, I. J., & Fenrich, F. R. (2010). Modeling ULF waves in a compressed dipole magnetic field. *Journal of Geophysical Research*, 115, A10212. <https://doi.org/10.1029/2010JA015410>
- D'haeseleer, W. D., Hitchon, W. N. G., Callen, J. D., & Shohet, J. L. (1991). *Flux coordinates and magnetic field structure*. Springer-Verlag.
- Dungey, J. W. (1954). *Electrodynamics of the outer atmosphere: Report to national science foundation on work carried on under grant nsf-g450*. Pennsylvania State University, Ionosphere Research Laboratory. Retrieved from <https://books.google.co.uk/books?id=3NrUAAAMAAJ>

- Ellington, S. M., Moldwin, M. B., & Liemohn, M. W. (2016). Local time asymmetries and toroidal field line resonances: Global magnetospheric modeling in SWMF. *Journal of Geophysical Research: Space Physics*, 121, 2033–2045. <https://doi.org/10.1002/2015JA021920>
- Elsden, T., & Wright, A. (2020). Evolution of high-m poloidal Alfvén waves in a dipole magnetic field. *Journal of Geophysical Research: Space Physics*, 125, e28187. <https://doi.org/10.1029/2020JA028187>
- Elsden, T., & Wright, A. N. (2017). The theoretical foundation of 3-D Alfvén resonances: Time-dependent solutions. *Journal of Geophysical Research: Space Physics*, 122, 3247–3261. <https://doi.org/10.1002/2016JA023811>
- James, M. K., Imber, S. M., Yeoman, T. K., & Bunce, E. J. (2019). Field line resonance in the hermean magnetosphere: Structure and implications for plasma distribution. *Journal of Geophysical Research: Space Physics*, 124, 211–228. <https://doi.org/10.1029/2018JA025920>
- Kabin, K., Rankin, R., Mann, I. R., Degeling, A. W., & Marchand, R. (2007). Polarization properties of standing shear Alfvén waves in non-axisymmetric background magnetic fields. *Annales Geophysicae*, 25, 815–822. <https://doi.org/10.5194/angeo-25-815-2007>
- Klimushkin, D. Y., Leonovich, A. S., & Mazur, V. A. (1995). On the propagation of transversally small-scale standing Alfvén waves in a three-dimensionally inhomogeneous magnetosphere. *Journal of Geophysical Research*, 100(A6), 9527–9534. <https://doi.org/10.1029/94JA03233>
- Lee, D.-H., & Lysak, R. L. (1989). Magnetospheric ULF wave coupling in the dipole model - The impulsive excitation. *Journal of Geophysical Research*, 94, 17097–17103. <https://doi.org/10.1029/JA094iA12p17097>
- Leonovich, A. S., & Mazur, V. A. (1993). A theory of transverse small-scale standing Alfvén waves in an axially symmetric magnetosphere. *Planetary and Space Science*, 41(9), 697–717. [https://doi.org/10.1016/0032-0633\(93\)90055-7](https://doi.org/10.1016/0032-0633(93)90055-7)
- Mager, P. N., & Klimushkin, D. Y. (2021). The field line resonance in the three dimensionally inhomogeneous magnetosphere: Principal features. *Journal of Geophysical Research: Space Physics*, 126, e28455. <https://doi.org/10.1029/2020JA028455>
- Mann, I. R., Wright, A. N., & Cally, P. S. (1995). Coupling of magnetospheric cavity modes to field line resonances: A study of resonance widths. *Journal of Geophysical Research*, 100, 19441–19456. <https://doi.org/10.1029/95JA00820>
- Rickard, G. J., & Wright, A. N. (1994). Alfvén resonance excitation and fast wave propagation in magnetospheric waveguides. *Journal of Geophysical Research*, 99, 13455. <https://doi.org/10.1029/94JA00674>
- Russell, A. J. B., & Wright, A. N. (2010). Resonant absorption with 2D variation of field line eigenfrequencies. *Astronomy and Astrophysics*, 511, A17. <https://doi.org/10.1051/0004-6361/200912669>
- Samson, J. C., Jacobs, J. A., & Rostoker, G. (1971). Latitude-dependent characteristics of long-period geomagnetic micropulsations. *Journal of Geophysical Research*, 76, 3675–3683. <https://doi.org/10.1029/JA076i016p03675>
- Singer, H. J., Southwood, D. J., Walker, R. J., & Kivelson, M. G. (1981). Alfvén wave resonances in a realistic magnetospheric magnetic field geometry. *Journal of Geophysical Research*, 86, 4589–4596. <https://doi.org/10.1029/JA086iA06p04589>
- Southwood, D. J. (1974). Some features of field line resonances in the magnetosphere. *Planetary and Space Science*, 22, 483–491. [https://doi.org/10.1016/0032-0633\(74\)90078-6](https://doi.org/10.1016/0032-0633(74)90078-6)
- Southwood, D. J., & Kivelson, M. G. (1981). Charged particle behavior in low-frequency geomagnetic pulsations 1. Transverse waves. *Journal of Geophysical Research*, 86(A7), 5643–5655. <https://doi.org/10.1029/JA086iA07p05643>
- Thompson, M. J., & Wright, A. N. (1993). Resonant Alfvén wave excitation in two-dimensional systems - Singularities in partial differential equations. *Journal of Geophysical Research*, 98, 15. <https://doi.org/10.1029/93JA00791>
- Wright, A. N. (1994). Dispersion and wave coupling in inhomogeneous MHD waveguides. *Journal of Geophysical Research*, 99, 159–167. <https://doi.org/10.1029/93JA02206>
- Wright, A. N., & Elsden, T. (2016). The theoretical foundation of 3D Alfvén resonances: Normal modes. *Astrophysical Journal*, 833, 230. <https://doi.org/10.3847/1538-4357/833/2/230>
- Wright, A. N., & Elsden, T. (2020). Simulations of MHD wave propagation and coupling in a 3-D magnetosphere. *Journal of Geophysical Research: Space Physics*, 125(2), e27589. <https://doi.org/10.1029/2019JA027589>
- Wright, A. N., & Thompson, M. J. (1994). Analytical treatment of Alfvén resonances and singularities in nonuniform magnetoplasmas. *Physics of Plasmas*, 1, 691–705. <https://doi.org/10.1063/1.870815>